GEOPHYSICS, VOL. 87, NO. 4 (JULY-AUGUST 2022); P. E205–E217, 9 FIGS., 1 TABLE.
10.1190/GEO2021-0216.1

Three-dimensional magnetotelluric modeling in a mixed space-wavenumber domain

Shikun Dai[1], Dongdong Zhao[2], Shunguo Wang[3], Kun Li[4], and Hormoz Jahandari[5]

ABSTRACT

We have developed a new 3D magnetotelluric modeling scheme in a mixed space-wavenumber domain. The modeling scheme is based on using a 2D Fourier transform along two horizontal directions to solve a vector-scalar potential formula derived from Maxwell's equations based on the primary-secondary potential separation. The derived 1D governing equations in a mixed space-wavenumber domain are solved by using the finite-element method (FEM) together with a chasing method, and then the 2D inverse Fourier transform is used to recover the final solution of the electromagnetic (EM) fields in the 3D spatial domain. An iterative scheme is applied to approximate the true solution by repeating the previous steps because the governing equations cannot be solved directly due to an unusual primary-secondary potential field separation used. Nevertheless, the new method is capable of reducing the memory requirement and computational time in the mixed domain, and the 1D governing equations are highly parallel among different wavenumbers. For each of the 1D equations, the two- or four-node Gaussian quadrature rule can be used in both horizontal directions for Gauss fast Fourier transform. It is worth mentioning that the linear matrix equation to be solved is a fixed bandwidth system, and the chasing method is more efficient and convenient than solvers with preconditioners for the 1D matrix equations. The reliability and efficiency of the newly proposed method are verified with three synthetic 3D models by comparisons with a classical integral equation solution, an adaptive FEM solution, and a nonadaptive FEM solution. The proposed algorithm will be used in electrical resistivity tomography and controlled-source EM methods in future studies.

INTRODUCTION

The magnetotelluric (MT) method plays an important role in various applications, such as crustal structure studies, environment investigation, and resource exploration. Highly efficient and accurate solutions of 3D large-scale electromagnetic (EM) equations become practical to simulate observations from geophysical surveys and then solve the EM inverse problem (Zhdanov, 2010). Many algorithms have been proposed for 3D MT modeling (e.g., Varentsov, 1983; Wannamaker et al., 1984a; Newman and Alumbaugh, 2000; Mitsuhata and Uchida, 2004; Egbert and Kelbert, 2012; Ren et al., 2013; Jahandari et al., 2017). From the perspective of solving the EM fields or their potentials, MT forward modeling can be cataloged into two types: (1) the EM-field approach (Mackie et al., 1994; Varilsuha and Candansayar, 2018) and (2) the potential approach (Um et al., 2010; Mukherjee and Everett, 2011; Jahandari and Farquharson, 2014, Varilsuha and Candansayar, 2018). Both approaches can accurately solve the relevant partial differential equations (PDEs) derived from Maxwell's equations with consideration of an appropriate boundary condition.

The EM-field approach solves the conventional EM Helmholtz equation consisting of either the electric or magnetic fields as unknown quantities in the spatial domain. The principle of this approach is relatively simple and straightforward, but the main drawback of the EM-field approach is that it will violate the divergence-free condition of current due to the accumulation of round-off errors if an iterative solver is used for simulations with low frequency (Lynch and Paulsen, 1991). However, the application of the vectorial finite-element

Manuscript received by the Editor 6 April 2021; revised manuscript received 30 January 2022; published ahead of production 19 March 2022; published online 13 May 2022.
[1]Central South University, School of Geosciences and Info-physics, Changsha, China. E-mail: dskgmes@csu.edu.cn.
[2]Guilin University of Electronic Technology, School of Electronic Engineering and Automation, Guilin, China. E-mail: dongzhaochd@163.com.
[3]Norwegian University of Science and Technology, Department of Electronic Systems, Trondheim, Norway. E-mail: wangshunguo@yeah.net (corresponding author).
[4]Southwest Petroleum University, School of Geoscience and Technology, Chengdu, China. E-mail: 546803024@qq.com.
[5]Memorial University of Newfoundland, Department of Earth Science, St. John's, Canada. E-mail: hormoz1486@gmail.com.

method (FEM) to the solutions of the E-field (Sugeng, 1998; Liu et al., 2008; Farquharson and Miensopust, 2011; Ren et al., 2013; Grayver and Kolev, 2015; Key, 2016) and H-field (Franke et al., 2007) diffusion equation overcomes those difficulties mentioned previously for the EM-field approach.

The potential approach that discretizes the EM problem based on a vector-scalar potential formulation instead of directly using electric and magnetic fields also has been suggested. Various gauge methods have been used in a vector-scalar potential formula, and the potential approach can be further divided into the ungauged approach (Mukherjee and Everett, 2011; Ansari and Farquharson, 2014), Coulomb-gauge approach (Haber et al., 2000; Jahandari and Farquharson, 2014), Lorenz-gauge approach (Um et al., 2010), and axial-gauge approach (Varilsuha and Candansayar, 2018). These approaches have two main features: (1) using vector and scalar potentials allows the divergence correction scheme to be included implicitly in the stiffness matrix and (2) there are more nonzero elements in the assembled large stiffness matrix compared with the EM-field approaches. Although the solutions of the vector and scalar potentials are not unique, the corresponding EM fields are unique in the ungauged case.

For either the EM-field approach or the vector-scalar potential approach, the integral equation (IE) method (e.g., Wannamaker et al., 1984b; Avdeev et al., 2002; Avdeev and Avdeeva, 2009; Kruglyakov and Bloshanskaya, 2017), finite-difference method (e.g., Varentsov, 1983; Mackie et al., 1994; Newman and Alumbaugh, 1995; Haber et al., 2000; Sasaki, 2001; Shen, 2003), finite-volume method (e.g., Haber et al., 2000; Haber and Ascher, 2001; Streich, 2009; Jahandari and Farquharson, 2014, 2015), and FEM (Zunoubi et al., 1999; Nam et al., 2007; Um et al., 2010; Mukherjee and Everett, 2011; Ren et al., 2013; Ansari and Farquharson, 2014; Jahandari et al., 2017) are often selected to solve the Helmholtz equations. Note that an explicit divergence correction is required when using the EM-field approach, and it not only ensures the conservation of currents inside an element but also speeds up the convergence process by reducing the number of iterations for the numerical solution (Mackie et al., 1994; Smith, 1996). Direct solvers (e.g., SuperLU and Multifrontal Massively Parallel Sparse direct Solver [MUMPS]) or iterative solvers (e.g., Portable Extensible Toolkit for Scientific Computation (PETSc) and generalized minimum residual method [GMRES]) can be selected to solve the assembled matrix equation, which also influences the calculation accuracy and efficiency (Saad, 2003; Streich, 2009; da Silva et al., 2012; Jahandari and Farquharson, 2014).

In 3D MT modeling, computation and memory requirements for field data are enormous, especially when a large-scale sparse linear system is solved. Therefore, regardless of whether one uses the EM-field approach or the potential approach, further development of the 3D MT modeling algorithm should focus on improving computational efficiency while preserving high accuracy. From the perspective of differential equations, we propose to carry out the 3D MT forward modeling by obtaining the solution in a mixed space-wavenumber domain based on the potential approach. This method has been used in gravity and magnetic modeling (Dai et al., 2019). Using the method, the 3D vector-scalar potential PDEs are converted into 1D governing equations with different independent wavenumbers by 2D Fourier transform along two horizontal directions in the Cartesian coordinate system. The 1D governing equations with different wavenumbers support parallel computation on high-performance computers. In the vertical dimension, the accuracy and the efficiency are balanced by increasing the mesh size as the depth increases. For the transformed 1D differential equations, the FEM combined with a chasing approach is applied for an accurate and efficient solution of 3D MT modeling. Because the total electric field is involved in the final matrix equation, an iterative approach is required to approximate the final solution. Three 3D models with different anomalies are used to verify the accuracy and the reliability of the proposed algorithm by comparisons between the proposed method and a classical IE method, a spatial domain adaptive FEM, and a spatial domain nonadaptive FEM.

BASIC THEORY

Gauged EM potentials

Assuming the time dependence of $e^{-i\omega t}$ in the frequency domain, the EM fields satisfy the Maxwell equations:

$$\nabla \times \mathbf{E} = i\omega\mu_0\mathbf{H}, \tag{1}$$

$$\nabla \times \mathbf{H} = \mathbf{J_S} + (\sigma - \mathrm{i}\omega\varepsilon)\mathbf{E}, \tag{2}$$

where $\mathbf{E}$ and $\mathbf{H}$ represent the electric field (V/m) and the magnetic field (A/m), respectively, in the frequency domain; ω represents angular frequency; i represents the imaginary unit; σ represents the conductivity (S/m); ε represents the dielectric permittivity (F/m); and $\mathbf{J_S}$ only represents the current density (A/m^2). Within the MT frequency band (approximately 10^{-5}–10^4 Hz), the displacement current is negligible, and the free-space magnetic permeability is $\mu_0 = 4\pi \times 10^{-7}$ H/m.

The electric field $\mathbf{E}$ can be described by a vector potential ($\mathbf{A}$) and a scalar potential (Φ) (Haber et al., 2000), where $\mathbf{A}$ is known as the magnetic potential and Φ is the electric potential. The value $\mathbf{A}$ is a vector perpendicular to the magnetic induction intensity $\mathbf{B}$:

$$\mathbf{B} = \nabla \times \mathbf{A}. \tag{3}$$

The electric field $\mathbf{E}$ then can be written in terms of the vector potential $\mathbf{A}$ and the scalar potential Φ as

$$\mathbf{E} = i\omega\mathbf{A} - \nabla\Phi. \tag{4}$$

In terms of the EM potentials, equation 2 can be written as the curl-curl equation:

$$\nabla \times (\nabla \times \mathbf{A}) = \mu_0\mathbf{J_S} + \mu_0\sigma(i\omega\mathbf{A} - \nabla\Phi). \tag{5}$$

Using the vector identity $\nabla \times (\nabla \times \mathbf{A}) = \nabla(\nabla \cdot \mathbf{A}) - \nabla^2\mathbf{A}$ and the Coulomb gauge condition of $\nabla \cdot \mathbf{A} = 0$ obtains that equation 5 is equivalent to

$$\nabla^2\mathbf{A} + k^2\mathbf{A} - \mu_0\hat{y}\nabla\Phi = -\mu_0\mathbf{J_S}, \tag{6}$$

where $k = \sqrt{i\omega\mu\sigma}$ is wavenumber in the frequency domain and $\hat{y} = \sigma$ represents the admittivity when the displacement current is negligible.

The divergence-free condition of the current density, $\mathbf{J} = \mathbf{J_S} + \sigma\mathbf{E}$, is satisfied as $\nabla \cdot \mathbf{J} = 0$. Thus, to maintain a divergence-free current density, the auxiliary equation can be written as

$$-\nabla \cdot \mathbf{J_S} = \nabla \cdot \sigma\mathbf{E}. \tag{7}$$

Through replacing the electric field with the $\mathbf{A} - \Phi$ combination in equation 4, equation 7 can be reformed into

$$\nabla \cdot (\sigma\nabla\Phi) - i\omega\nabla \cdot (\sigma\mathbf{A}) = \nabla \cdot \mathbf{J_S}. \tag{8}$$

The system of equations for the vector potential $\mathbf{A}$ and scalar potential Φ can be composed of equations 6 and 8 (Haber et al., 2000; Badea et al., 2001) as

$$\begin{cases} \nabla^2\mathbf{A} + k^2\mathbf{A} - \mu_0\sigma\nabla\Phi = -\mu_0\mathbf{J_S} \\ \nabla \cdot (\sigma\nabla\Phi) - i\omega\nabla \cdot (\sigma\mathbf{A}) = \nabla \cdot \mathbf{J_S} \end{cases}. \tag{9}$$

Equation 9 should be solved simultaneously as a coupled matrix equation. There is no gauge freedom after applying Coulomb gauge in this system because the solution's vector potential $\mathbf{A}$ and scalar potential Φ are unique, unlike the ungauged system (Varilsuha and Candansayar, 2018). The equations of $\mathbf{A}$ and Φ can be used for 3D forward modeling of MT, electrical resistivity tomography (ERT), and controlled-source electromagnetic (CSEM) methods by tuning the current density and frequency selection. Meanwhile, only 3D MT modeling is presented in this study to illustrate the methodology, and the $\mathbf{J_S}$ term is neglected.

When a secondary potential formulation is used to model MT signals, plane waves can be introduced conveniently by explicitly calculating a set of known primary EM potentials ($\mathbf{A}^p$, Φ^p). The primary potentials can be the responses of a half-space or layered electrical resistivity model. The disadvantage of the secondary EM potentials algorithm is that it cannot be easily used for topography inclusion in 3D EM simulation due to the lack of a direct solution of the relevant primary potentials.

The equation of the primary EM potentials ($\mathbf{A^p}$, $\Phi^\mathbf{p}$) can be described as

$$\begin{cases} \nabla^2\mathbf{A^p} + k_p^2\mathbf{A^p} - \mu_0\sigma^p\nabla\Phi^\mathbf{p} = -\mu_0\mathbf{J_S} \\ \nabla \cdot (\sigma^p\nabla\Phi^\mathbf{p}) - i\omega\nabla \cdot (\sigma^p\mathbf{A^p}) = \nabla \cdot \mathbf{J_S} \end{cases}. \tag{10}$$

The secondary EM potentials ($\mathbf{A^s}$,$\Phi^\mathbf{s}$) can be defined according to $\mathbf{A} = \mathbf{A^p} + \mathbf{A^s}$ and $\Phi = \Phi^\mathbf{p} + \Phi^\mathbf{s}$. Then, by subtracting the primary potentials from the total potentials, the governing equation 9 can be rewritten as

$$\begin{cases} \nabla^2\mathbf{A^s} + k_p^2\mathbf{A^s} - \mu_0\sigma^p\nabla\Phi^\mathbf{s} = -\mu_0\sigma^s\mathbf{E} \\ \nabla \cdot (\sigma^p\nabla\Phi^\mathbf{s}) - i\omega\nabla \cdot (\sigma^p\mathbf{A^s}) = \nabla \cdot (\sigma^s\mathbf{E}) \end{cases}. \tag{11}$$

Here,

$$\begin{cases} k^2 = k_p^2 + k_s^2 \\ \sigma = \sigma^p + \sigma^s \end{cases}, \tag{12}$$

where k_p^2 and k_s^2 are the wavenumbers corresponding to the primary and secondary EM potentials, respectively. Similarly, σ^p and σ^s are the conductivity corresponding to the primary and secondary EM potentials, respectively. The $\mathbf{E} = \mathbf{E}^p + \mathbf{E}^s$ is the total electric field, where $\mathbf{E}^p$ is the primary field and $\mathbf{E}^s$ is the second field. In the process of solving equation 11 for the first iteration, only plane EM waves $\mathbf{E}^p$ are used to represent $\mathbf{E}$, and the initial value of the secondary field $\mathbf{E}^s$ is zero. Then, the total field $\mathbf{E}$ on the right side of equation 11 can be updated iteratively with the sum of the secondary field $\mathbf{E}^s$ and the primary field $\mathbf{E}^p$. The details of the iterative method are shown at the end of this section. Equation 11 is different from the conventional equation used for primary and secondary potential separation. This is because the conventional equation contains the product of total conductivity and secondary potential field (e.g., Badea et al., 2001; Chen and Li, 2019), which results to complicate convolution after the Fourier transform.

Equations 9 and 11, as well as their equivalent equations, have been used in several studies (e.g., Haber et al., 2000, Badea et al., 2001, Jahandari and Farquharson, 2015). However, the computational cost and memory requirements are large (Varilsuha and Candansayar, 2018) due to the direct solver of the large sparse matrix equation. This study proposes a new 3D MT modeling method in a mixed space-wavenumber domain based on equation 11. This simulation method mainly includes four steps starting from equation 11: (1) use the 2D Fourier transform along two horizontal directions; (2) use the 1D FEM to solve 1D differential equations with respect to the secondary EM potentials ($\mathbf{A^s}$, $\Phi^\mathbf{s}$) in the mixed space-wavenumber domain; (3) iteratively update the electric field with a contraction operator until convergence; and (4) recover the EM fields and other parameters, such as the impedance tensor, in the spatial domain. To be specific, we transform x and y from the spatial domain into the wavenumber domain using Fourier transform regarding equation 11; then, only the vertical direction z is preserved in the spatial domain. The 3D vector-scalar potential equations are simplified into 1D equations. The given 1D independent differential equations can be computed in parallel among different wavenumbers, which improves the efficiency of 3D MT numerical simulation through parallelization. The FEM is used to solve the 1D equations of the secondary EM potentials ($\mathbf{A^s}$, $\Phi^\mathbf{s}$) subjected to different wavenumbers. Meanwhile, a contraction operator based on the series expansion is used to iteratively update the secondary electric field until the field cannot be further updated. This is because the initial total electric field in equation 11 is calculated with a half-space model, so that the primary field was used to represent the total field at the first iteration. Then, the iteration lasts until the secondary electric field cannot be further updated. After the calculation of the secondary electric field is done, the secondary magnetic field can be recovered through the corresponding potential $\mathbf{A^s}$. Finally, using inverse fast Fourier transform (FFT), we can add the secondary fields to the spatial primary EM fields to give the solution of 3D MT modeling in the spatial domain.

Governing equations in the mixed domain

By using the Coulomb gauge condition, equation 11 can be written into subequations in the Cartesian coordinate system as

$$\begin{cases} \frac{\partial^2 A_x^s}{\partial x^2}+\frac{\partial^2 A_x^s}{\partial y^2}+\frac{\partial^2 A_x^s}{\partial z^2}+k_p^2 A_x^s-\mu_0\sigma^p\frac{\partial \Phi^s}{\partial x}=-\mu_0 j_x^s \\ \frac{\partial^2 A_y^s}{\partial x^2}+\frac{\partial^2 A_y^s}{\partial y^2}+\frac{\partial^2 A_y^s}{\partial z^2}+k_p^2 A_y^s-\mu_0\sigma^p\frac{\partial \Phi^s}{\partial y}=-\mu_0 j_y^s \\ \frac{\partial^2 A_z^s}{\partial x^2}+\frac{\partial^2 A_z^s}{\partial y^2}+\frac{\partial^2 A_z^s}{\partial z^2}+k_p^2 A_z^s-\mu_0\sigma^p\frac{\partial \Phi^s}{\partial z}=-\mu_0 j_z^s \\ \sigma^p\left(\frac{\partial^2 \Phi^s}{\partial x^2}+\frac{\partial^2 \Phi^s}{\partial y^2}+\frac{\partial^2 \Phi^s}{\partial z^2}\right)+\frac{\partial \Phi^s}{\partial z}\frac{\partial \sigma^p}{\partial z}-i\omega A_z^s\frac{\partial \sigma^p}{\partial z} \\ =\frac{\partial j_x^s}{\partial x}+\frac{\partial j_y^s}{\partial y}+\frac{\partial j_z^s}{\partial z} \end{cases}, \quad (13)$$

where $j_x^s=\sigma^s E_x$, $j_y^s=\sigma^s E_y$, and $j_z^s=\sigma^s E_z$ are current density in three different directions, respectively.

In two horizontal directions, we transform spatially related parameters into the wavenumber domain. Then, we obtain

$$\begin{cases} \frac{\partial^2 \tilde{A}_x^s}{\partial z^2}+(k_p^2-k_x^2-k_y^2)\tilde{A}_x^s+ik_x\mu_0\tilde{\sigma}^p\tilde{\Phi}^s=-\mu_0\tilde{j}_x^s \\ \frac{\partial^2 \tilde{A}_y^s}{\partial z^2}+(k_p^2-k_x^2-k_y^2)\tilde{A}_y^s+ik_y\mu_0\tilde{\sigma}^p\tilde{\Phi}^s=-\mu_0\tilde{j}_y^s \\ \frac{\partial^2 \tilde{A}_z^s}{\partial z^2}+(k_p^2-k_x^2-k_y^2)\tilde{A}_z^s-\tilde{\sigma}^p\mu_0\frac{\partial \tilde{\Phi}^s}{\partial z}=-\mu_0\tilde{j}_z^s \\ \left(\tilde{\sigma}^p\frac{\partial^2 \tilde{\Phi}^s}{\partial z^2}+\frac{\partial \tilde{\sigma}^p}{\partial z}\frac{\partial \tilde{\Phi}^s}{\partial z}-\tilde{\sigma}^p(k_x^2+k_y^2)\tilde{\Phi}^s\right) \\ -i\omega\tilde{A}_z^s\frac{\partial \tilde{\sigma}^p}{\partial z}=-ik_x\tilde{j}_x^s-ik_y\tilde{j}_y^s+\frac{\partial \tilde{j}_z^s}{\partial z} \end{cases}, \quad (14)$$

where the symbol ˜ marks parameters in a mixed space-wavenumber domain (Table 1) and k_x and k_y are the wavenumbers in the mixed domain. Similar to 3D modeling of gravity and magnetic anomalies in a mixed space-wavenumber domain (Dai et al., 2019), equation 14 describes the vector-scalar potentials governing equations for 3D MT modeling with different wavenumbers in the mixed domain after 2D Fourier transform along the horizontal x- and y-directions. The selection of wavenumber with the Gauss FFT method is based on the shift-sampling technique and Gaussian quadrature rule (Wu and Tian, 2014), and it can efficiently overcome the imposed periodicity and edge effect caused by FFT (Chai, 2009). Gauss FFT with a two- or four-node Gaussian quadrature rule has been proven to support a solution equivalent to a solution computed in the space domain (Wu and Tian, 2014; Dai et al., 2019).

Through the preceding detailed formula derivation, a large-scale 3D complex EM equation system is transformed into a small-scale 1D simple EM equation system that is decoupled in horizontal wavenumber and amenable to fully parallel computation. Thus, this 3D numerical modeling can be carried out on a multiple-core or a multiple-CPU computer with open multiprocessing (OpenMP). It is useful for large-scale EM surveys due to the reduction of memory demand. To solve equation 14, we have to iteratively update EM fields, for the reason mentioned.

Table 1. The symbols used for different parameters in the spatial domain and the mixed space-wavenumber domain are listed.

Parameter name	Spatial domain	Mixed domain
Electric field	$\mathbf{E}$	$\tilde{\mathbf{E}}$
Primary electric field	$\mathbf{E}^p$	$\tilde{\mathbf{E}}^p$
Secondary electric field	$\mathbf{E}^s$	$\tilde{\mathbf{E}}^s$
Magnetic field	$\mathbf{H}$	—
Magnetic induction intensity	$\mathbf{B}$	—
Current density	$\mathbf{J}_s$	—
Vector potential	$\mathbf{A}$	—
Scalar potential	Φ	—
Fourier wavenumbers	—	k_x, k_y
Frequency wavenumbers	k_p, k_s	—
Primary vector potential	$\mathbf{A}^p$, Φ^p	—
Secondary vector potential	$\mathbf{A}^s$	$\tilde{\mathbf{A}}^s$
Secondary scalar potential	Φ^s	$\tilde{\Phi}^s$
Components of the secondary vector potential	A_x^s, A_y^s, A_z^s	$\tilde{A}_x^s$, $\tilde{A}_y^s$, $\tilde{A}_z^s$
Components of current density	j_x^s, j_y^s, j_z^s	$\tilde{j}_x^s$, $\tilde{j}_y^s$, $\tilde{j}_z^s$
Primary conductivity	σ^p	$\tilde{\sigma}^p$
Secondary conductivity	σ^s	$\tilde{\sigma}^s$

Boundary conditions

In a source-free region, the boundary conditions for the secondary EM potentials ($\tilde{\mathbf{A}}^s$, $\tilde{\Phi}^s$) in the mixed space-wavenumber domain used in the modeling are shown as equations 15 and 16 (see more details in Appendix A):

$$\begin{cases} \frac{\partial \tilde{A}_x^s}{\partial z}=-s\tilde{A}_x^s+\frac{(t-s)}{\omega}k_x\tilde{\Phi}^s \\ \frac{\partial \tilde{A}_y^s}{\partial z}=-s\tilde{A}_y^s+\frac{(t-s)}{\omega}k_y\tilde{\Phi}^s \\ \frac{\partial \tilde{A}_z^s}{\partial z}=ik_x\tilde{A}_x^s+ik_y\tilde{A}_y^s \\ \frac{\partial \tilde{\Phi}^s}{\partial z}=-t\tilde{\Phi}^s \end{cases} \quad (15)$$

and

$$\begin{cases} \frac{\partial \tilde{A}_x^s}{\partial z}=s\tilde{A}_x^s-ik_x\tilde{A}_z^s+\frac{sk_x\tilde{\Phi}^s}{\omega} \\ \frac{\partial \tilde{A}_y^s}{\partial z}=s\tilde{A}_y^s-ik_y\tilde{A}_z^s+\frac{sk_y\tilde{\Phi}^s}{\omega} \\ \frac{\partial \tilde{A}_z^s}{\partial z}=ik_x\tilde{A}_x^s+ik_y\tilde{A}_y^s \\ \frac{\partial \tilde{\Phi}^s}{\partial z}=i\omega\tilde{A}_z^s \end{cases}, \quad (16)$$

where $s^2=k_x^2+k_y^2-k^2$ and $t^2=k_x^2+k_y^2$ are used for convenience. The Gauss FFT method can efficiently overcome the imposed periodicity and edge effect. Therefore, the boundary conditions in the horizontal direction are automatically satisfied without extra consideration.

FEM

The FEM with second-order interpolation (Xu, 1994; Jin, 2015) is an accurate approach to numerically solve the 1D governing equation in the mixed domain. Equations 14–16 are the 1D boundary value problems that the secondary EM potentials ($\tilde{\mathbf{A}}^s$, $\tilde{\Phi}^s$) satisfy. The mesh in the vertical direction can increase with depth due to the diffusive nature of the EM fields, so that the accuracy and efficiency can be guaranteed simultaneously. With a chasing method (Temperton, 1975; Boisvert, 1991; Dai et al., 2019), it is possible to solve the matrix equation assembled by finite-element analysis with a low cost even for a large-scale stiffness matrix.

The discrete finite element governing equations are derived with Galerkin's weighted residual method (Xu, 1994; Jin, 2015) in the mixed space-wavenumber domain, and the specific expressions are shown as (see more details in Appendix B)

$$\begin{cases} \sum_{e=1}^{Ne}\int_e\left(-\frac{\partial\tilde{A}_x^s}{\partial z}\frac{\partial N_i}{\partial z}+(k_p^2-k_x^2-k_y^2)N_i\tilde{A}_x^s+ik_x\mu_0\tilde{\sigma}^pN_i\tilde{\Phi}^s+N_i\mu_0\tilde{j}_x^s\right)dz \\ +\sum_{e=1}^{Ne}\int_s N_i\frac{\partial\tilde{A}_x^s}{\partial z}n_z dz=0 \\ \sum_{e=1}^{Ne}\int_e\left(-\frac{\partial\tilde{A}_y^s}{\partial z}\frac{\partial N_i}{\partial z}+(k_p^2-k_x^2-k_y^2)N_i\tilde{A}_y^s+ik_y\mu_0\tilde{\sigma}^pN_i\tilde{\Phi}^s+N_i\mu_0\tilde{j}_y^s\right)dz \\ +\sum_{e=1}^{Ne}\int_s N_i\frac{\partial\tilde{A}_y^s}{\partial z}n_z dz=0 \\ \sum_{e=1}^{Ne}\int_e\left(-\frac{\partial\tilde{A}_z^s}{\partial z}\frac{\partial N_i}{\partial z}+(k_p^2-k_x^2-k_y^2)N_i\tilde{A}_z^s-\mu_0\tilde{\sigma}^pN_i\frac{\partial\tilde{\Phi}^s}{\partial z}+N_i\mu_0\tilde{j}_z^s\right)dz \\ +\sum_{e=1}^{Ne}\int_s N_i\frac{\partial\tilde{A}_z^s}{\partial z}n_z dz=0 \\ \sum_{e=1}^{Ne}\int_e\left(-\tilde{\sigma}^p\frac{\partial\tilde{\Phi}^s}{\partial z}\frac{\partial N_i}{\partial z}+N_i\frac{\partial\tilde{\sigma}^p}{\partial z}\frac{\partial\tilde{\Phi}^s}{\partial z}-\tilde{\sigma}^p(k_x^2+k_y^2)N_i\tilde{\Phi}^s\right)dz+ \\ \sum_{e=1}^{Ne}\int_e\left(-i\omega N_i\frac{\partial\tilde{\sigma}^p}{\partial z}\tilde{A}_z^s+ik_xN_i\tilde{j}_x^s+ik_yN_i\tilde{j}_y^s-N_i\frac{\partial\tilde{j}_z^s}{\partial z}\right)dz+ \\ \sum_{e=1}^{Ne}\int_s\tilde{\sigma}^pN_i\frac{\partial\tilde{\Phi}^s}{\partial z}n_z dz=0 \end{cases} \tag{17}$$

where e represents the index of the elements, N_e is the number of the total elements, N_i represents the shape function, and n_z represents the normal vector. The mesh used in the study is structured.

In the z-direction (Figure 1), a second-order shape function is used in the elements. As a result, the secondary vector potential $\tilde{\mathbf{A}}^s$ and the secondary scalar potential $\tilde{\Phi}^s$ have two values in each element along the z-direction. Finally, a full stiffness matrix equation system is assembled by finite-element analysis as (see more details in Appendix C):

$$\mathbf{K}_{nz\times4\times23}\mathbf{u}_{nz\times4}=\mathbf{P}_{nz\times4}, \tag{18}$$

where the subscript nz is the number of vertical grid nodes, $\mathbf{u}$ is the unknown vector potential and scalar potential, $\mathbf{K}$ is a symmetric diagonal matrix with 23 rows in each cell, and $\mathbf{P}$ is a vector. The linear matrix equation to be solved is a fixed bandwidth system, and the chasing method selected is more efficient and convenient than solvers with preconditioners. Then, the secondary EM potentials ($\tilde{\mathbf{A}}^s$, $\tilde{\Phi}^s$) can be obtained in the mixed domain. Although we have to simultaneously solve the potentials at every node, the recovery of the fields in the spatial domain only involves the observational locations and their neighbor nodes.

EM field components

Equations 3 and 4 can be decomposed into three subequations in the spatial domain, respectively:

$$\begin{cases} E_x=i\omega A_x-\frac{\partial\Phi}{\partial x} \\ E_y=i\omega A_y-\frac{\partial\Phi}{\partial y} \\ E_z=i\omega A_z-\frac{\partial\Phi}{\partial z} \end{cases}, \tag{19}$$

$$\begin{cases} H_x=\frac{1}{\mu_0}\left(\frac{\partial A_z}{\partial y}-\frac{\partial A_y}{\partial z}\right) \\ H_y=\frac{1}{\mu_0}\left(\frac{\partial A_x}{\partial z}-\frac{\partial A_z}{\partial x}\right) \\ H_z=\frac{1}{\mu_0}\left(\frac{\partial A_y}{\partial x}-\frac{\partial A_x}{\partial y}\right) \end{cases}. \tag{20}$$

The utilization of the vector potential $\mathbf{A}$ and the electric potential Φ with the Coulomb gauge renders clear physical meanings, which is shown in equations 19 and 20. The vector potential is associated with currents and accumulated charges at various boundaries; however, the electric potential is only associated with accumulated charges. If one applies our modeling strategy to ERT, the $\mathbf{E}$ fields would only have the electric potential remaining in equation 19.

Using Fourier transform on equations 19 and 20 along two horizontal directions, the secondary EM fields in the mixed space-wavenumber domain then satisfy the following equations:

$$\begin{cases} \tilde{E}_x=i\omega\tilde{A}_x+ik_x\tilde{\Phi} \\ \tilde{E}_y=i\omega\tilde{A}_y+ik_y\tilde{\Phi} \\ \tilde{E}_z=i\omega\tilde{A}_z-\partial\tilde{\Phi}/\partial z \end{cases}, \tag{21}$$

$$\begin{cases} \tilde{H}_x=\frac{1}{\mu_0}\left(-ik_y\tilde{A}_z-\frac{\partial\tilde{A}_y}{\partial z}\right) \\ \tilde{H}_y=\frac{1}{\mu_0}\left(\frac{\partial\tilde{A}_x}{\partial z}+ik_x\tilde{A}_z\right) \\ \tilde{H}_z=\frac{1}{\mu_0}(-ik_x\tilde{A}_y+ik_y\tilde{A}_x) \end{cases}, \tag{22}$$

where $\partial\tilde{\Phi}/\partial z$, $\partial\tilde{A}_x/\partial z$, and $\partial\tilde{A}_y/\partial z$ can be obtained using the method of Jin (2015). When equation 18 is solved, the secondary vector potential $\tilde{\mathbf{A}}^s$ and the secondary scalar potential $\tilde{\Phi}^s$ and their derivatives can be used to calculate the secondary EM fields. Afterward, the 2D inverse Fourier transform is used to recover the fields in the spatial domain (Tontini et al., 2009; Wu and Tian, 2014). With the addition of the primary field, the total EM fields and impedance tensor can be calculated.

Electric field iteration in the spatial domain

The primary electric field rather than the total electric field is used to solve equation 11 for the first step; then, an approach similar to the Born approximation is used to iteratively reduce the inaccuracy of the secondary electric field solved by 1D FEM in the mixed domain. To achieve a stable and accurate solution for the EM fields, an iterative method used in the IE is adopted to update the secondary electric field and then the total field until the total $\mathbf{E}$ field cannot be further updated.

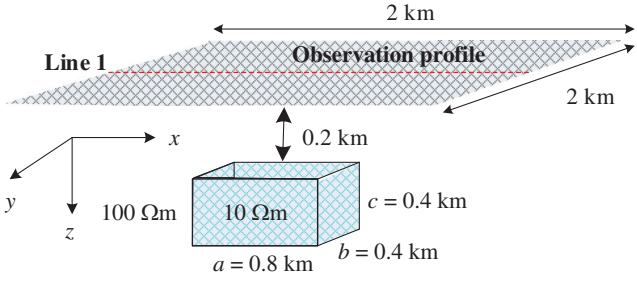

Figure 1. Synthetic resistivity model. A 10 Ωm anomaly is buried at 0.2 km depth in a 100 Ωm half-space model. The model region is 2 km^3 × 2 km^3 × 0.7 km^3, and the volume of the conductive anomaly is 0.8 km^3 × 0.4 km^3 × 0.4 km^3. The resistivities of the background half-space, the anomaly, and the air are 100, 10, and 108 Ωm, respectively.

Based on the Green's function of the electric field, the electric field IE can be written as (Avdeev et al., 1997; Hursán and Zhdanov, 2002)

$$\mathbf{E}(\mathbf{r}_j) = \mathbf{E}^{\mathbf{p}}(\mathbf{r}_j) + G[\Delta\sigma(\mathbf{r}) \cdot \mathbf{E}(\mathbf{r})], \tag{23}$$

where $\mathbf{E}$ is the total field; $\mathbf{E}^{\mathbf{p}}$ is the primary field; $\Delta\sigma$ is abnormal conductivity; $\mathbf{r}_j$ and $\mathbf{r}$ represent receiver position and anomaly position, respectively; and $G(\cdot)$ is a linear operator of

$$G(\cdot) = \iiint_V \bar{\mathbf{G}}(\mathbf{r}, \mathbf{r}')dv, \tag{24}$$

where $\bar{\mathbf{G}}(\mathbf{r}, \mathbf{r}')$ is the Green's function of the electric field.

The iterative method can be used to solve equation 23 in the form of

$$\mathbf{E}^{(n)} = \mathbf{E}^{\mathbf{p}} + G[\Delta\sigma \cdot \mathbf{E}^{(n-1)}]. \tag{25}$$

The Banach theorem (Gao, 2005) in functional analysis shows that the convergence condition for equation 25 is

$$\|G(\Delta\sigma \cdot (\mathbf{E}^{(n-1)} - \mathbf{E}^{(n)}))\| < \kappa\|\Delta\sigma \cdot (\mathbf{E}^{(n-1)} - \mathbf{E}^{(n)})\|, \tag{26}$$

where the iterative coefficient $\kappa < 1$ is required and $\|\cdot\|$ represents the L_2 norm. Thus, the condition that satisfies this equation is

$$\|G\| < 1. \tag{27}$$

The operator G, with contraction feature, is modified based on the energy inequality (Hursán and Zhdanov, 2002; Gao, 2005), and then the following iterative scheme is constructed to satisfy the requirement of the operator G:

$$\mathbf{E}^{(n)} = \alpha\mathbf{E}^{(n)} + \beta\mathbf{E}^{(n-1)}, \tag{28}$$

where

$$\alpha = \frac{2\sigma^p}{2\sigma^p + \boldsymbol{\Delta\sigma}}, \tag{29}$$

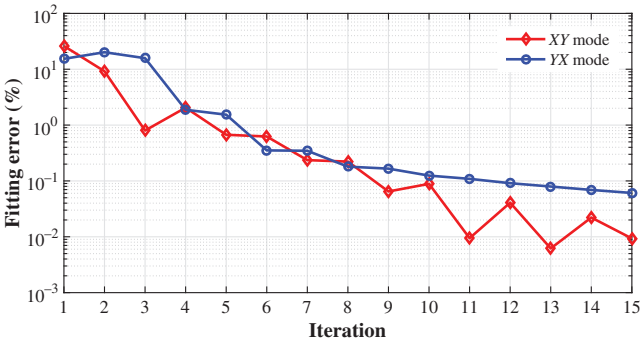

Figure 2. The fitting error against iteration number for the iterative approximation of the electric field. The *YX* mode (*y*-direction polarization) seems more stable than the *XY* mode (*x*-direction polarization).

$$\beta = \frac{\boldsymbol{\Delta\sigma}}{2\sigma^p + \boldsymbol{\Delta\sigma}}, \tag{30}$$

in which σ^p represents background conductivity, $\boldsymbol{\Delta\sigma}$ represents the anomalous conductivity, $\mathbf{E}^{(n)}$ represents the secondary electric field calculated with equation 21 in addition with the primary electric field, and $\mathbf{E}^{(n-1)}$ represents the value from the previous iteration (set as zero for the first iteration). The iterative relationship is used to update the right side of equation 11 to approximate an accurate solution. After the finite-element (FE) solution, we recover the total field $\mathbf{E}$ in the spatial domain and then update the total field $\mathbf{E}$ with equation 28. The updated $\mathbf{E}$-field is transformed into the Fourier domain before the FE matrix is solved again.

RESULTS

Model 1: Comparison with IE algorithm

The cuboid model shown in Figure 1 is used to evaluate the accuracy of 3D MT modeling. The proposed algorithm can be implemented with either the Gauss FFT method or the standard FFT method with grid expansion (Dai et al., 2019). As previously studied (see details in Dai et al., 2019), the Gauss FFT and the standard FFT have advantages and disadvantages with respect to accuracy and efficiency. In particular, when the model is discretized into a large number of elements, the standard FFT method with sufficient grid expansion is a good option; otherwise, the Gauss FFT method is a preferred option. The grid expansion requires several attempts to set up the expansion area to guarantee the accuracy. However, it is not straightforward to model field data with different tests of the grid expansion; the Gauss FFT is used in this study.

The model region is 2 km^3 × 2 km^3 × 0.7 km^3 and discretized into 51 × 51 × 75 nodes. However, the first two numbers, 51 × 51, represent the number of wavenumbers (the same as other examples). It contains 10 grid points in the vertical direction in the air layer. The frequencies selected are 0.01, 0.1, 1, and 10 Hz. The volume of a conductive anomaly is 0.8 km^3 × 0.4 km^3 × 0.4 km^3, and the top of the anomaly is located at 0.2 km depth. The resistivities of the homogeneous half-space, anomaly, and air are 100, 10, and 10^8 Ωm, respectively.

The new approach combined with the iterative scheme is applied to compute the EM fields. The machine used for calculation has four Intel(R) i7 cores with 2.60 GHz main frequency and 8 GB memory. The programming language is Fortran, and the Fortran code is parallelized with OpenMP.

To verify the accuracy of the final solution, the calculated responses of the designed model are compared with responses of the IE solution given by Hursán and Zhdanov (2002). The variation of iteration fitting errors against iteration number is shown in Figure 2. The fitting errors of *XY* mode (*x*-direction polarization) and *YX* mode (*y*-direction polarization) are less than 0.1% after 10 iterations, and the convergence of *YX* mode is more stable than *XY* mode due to the noncentrosymmetry of the cuboid anomaly. The simulation in this study iterates 15 times in total. The responses at 10 Hz obtained from the proposed algorithm using the Gauss FFT method with the four-node Gaussian quadrature rule are compared with the responses of the IE algorithm in detail (Figure 3). Their relative differences of $|V_{\text{new}} - V_{\text{IE}}|/V_{\text{IE}}$ on the plane of $z = 0$ also are shown (Figure 3). The response differences between the two methods are less than 0.6% (Figure 3), which is generally

smaller than the error floor of field data. Moreover, the phase data have even smaller relative differences than the apparent resistivity data. The relative differences of apparent resistivities and phases along a selected profile, marked as the red line in Figure 1, are shown in Figure 4. The responses of the four different frequencies are compared with each other. The relative differences of apparent resistivity and phase for 0.01, 0.1, and 1 Hz frequency are smaller than the differences for 10 Hz (Figure 4a–4d). Again, the relative differences in the phases are smaller than the relative differences in apparent resistivities. Therefore, the accuracy of the proposed algorithm is reasonable. The computation time for the *XY* mode and *YX* mode at 10 Hz is 44 s using the proposed method. However, the executable code of the IE algorithm is run with MATLAB, which can slow down the efficiency of the IE algorithm. Thus, the calculation time of the IE algorithm is not further analyzed. Instead, the calculation efficiency is studied in the following examples by comparing our algorithm with other FEM algorithms (Ren et al., 2013; Jahandari and Farquharson, 2017).

Model 2: Comparison with an adaptive FEM algorithm

A 3D model modified after Zhdanov et al. (2006) is used to further evaluate the 3D MT modeling accuracy. The model region is discretized into 101 × 101 × 71 nodes including 10 grid points in the vertical direction in the air layer (Figure 5). The frequency tested is 0.1 Hz. Two anomalies, one conductor and one resistor, are buried in a half-space model. The volume of each anomaly is 0.4 km^3 × 0.4 km^3 × 0.4 km^3, and the top of the anomaly is located at 0.2 km depth (Figure 5). The resistivities of the homogeneous half-space, conductive anomaly, resistive anomaly, and air are 100, 10, 1000, and 10^8 Ωm, respectively.

The solution of our method is compared to the adaptive FEM solution given by Ren et al. (2013) based on the same anomaly settings. The responses at 0.1 Hz calculated using the Gauss FFT method with the four-node Gaussian quadrature rule are plotted together with the responses at the same frequency from the adaptive FEM algorithm (Figure 6). The proposed algorithm iterates 15 times in total. The reference algorithm also iterates 15 times. However, the purposes of the iterations are different in the two algorithms. The former is due to the inaccurate total **E** field used to solve equation 11; the latter is due to the refinement of the FE grids. Because the algorithm of Ren et al. (2013) has been well tested, the results of the algorithm are treated as a reference solution. Clearly, the two results are very similar to each other (Figure 6a–6d). The relative differences of the two results $(V_{new} - V_{FEM})/V_{FEM}$ on the plane of $z = 0$ are shown in Figure 6e–6h. The relative differences are in general within 5% except at a few data points, which are smaller than the typical error floor of

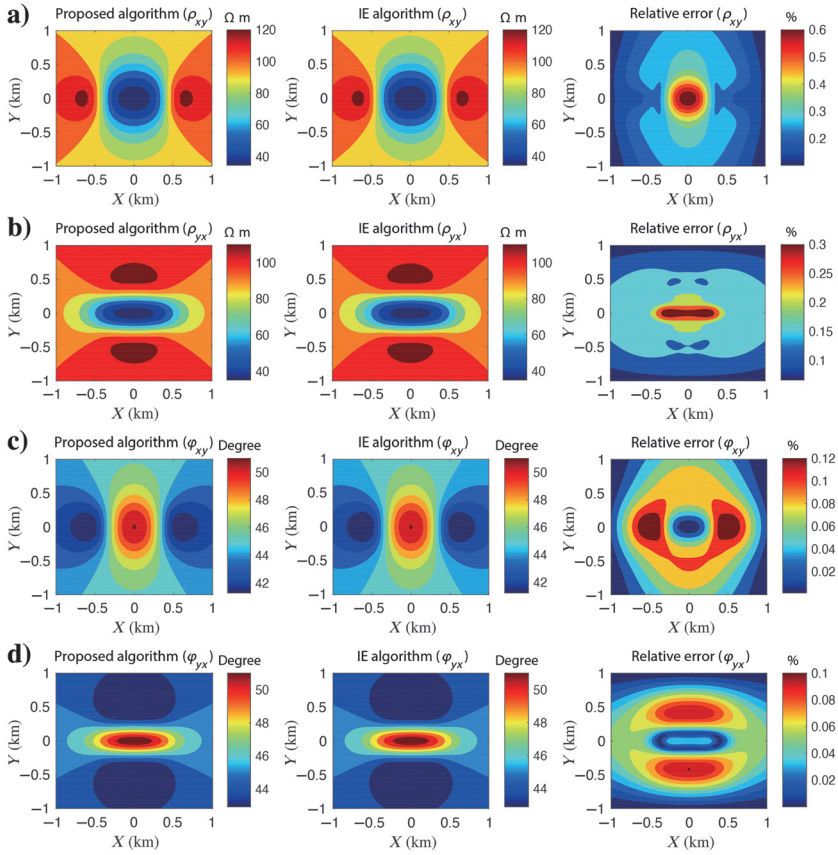

Figure 3. Apparent resistivities and phases at the frequency of 10 Hz calculated via the proposed algorithm, IE algorithm, and relative differences of the two along the plane of $z = 0$: (a) ρ_{xy}, (b) ρ_{yx}, (c) φ_{xy}, and (d) φ_{yx}. The relative differences are smaller than typical noise levels in field data.

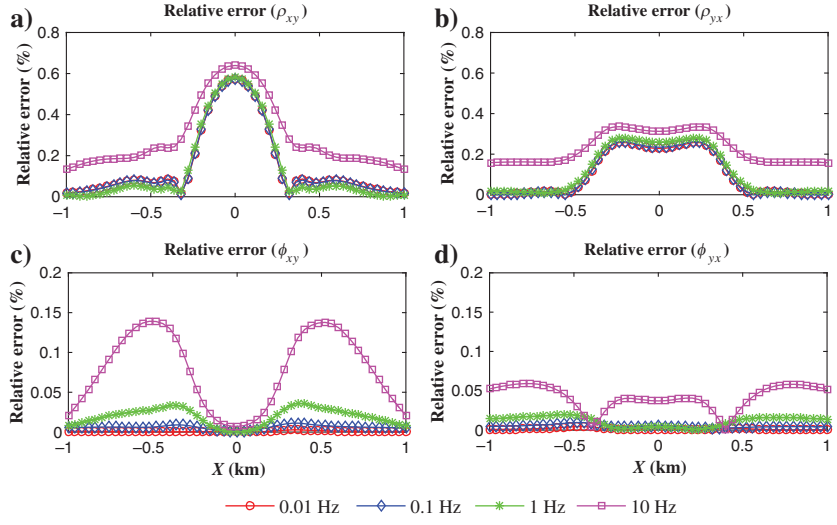

Figure 4. The relative differences of apparent resistivities and phases along the central profile marked in Figure 1: (a) ρ_{xy}, (b) ρ_{yx}, (c) φ_{xy}, and (d) φ_{yx}.

MT field data. Moreover, the phase data show smaller relative differences than the apparent resistivity data. Therefore, the accuracy of the proposed algorithm is reasonable.

The calculation time of our method is 143 s, which is 1199 s less than the calculation time of the adaptive FEM after 15 iterations in total. However, the calculation time for the 15th iteration of the adaptive FEM is only 151 s, which is slightly slower than the time required by our method. One should note that, without the previous 14 iterations, the final optimal mesh at the 15th iteration would not be easy to obtain. The maximum memory usage of our algorithm is 0.44 GB, which is 7 GB less than the one used for the adaptive FEM at the 15th iteration. The calculations have been performed with four cores, and two anomalies have been introduced in the model; that is why the calculation time with Ren et al. (2013) is longer than the time in the original publication. By analyzing the calculation time for this two-anomaly model and a one-anomaly model with our method and the adaptive FEM of Ren et al. (2013), respectively, we can estimate that approximately 70% of the increased calculation time is caused by the increased model complexity.

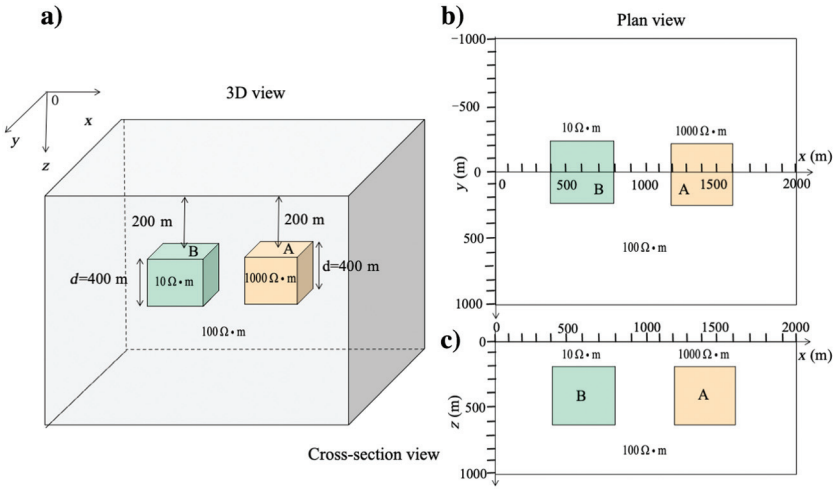

Figure 5. The 3D model modified after Zhdanov et al. (2006). The volume of each anomaly is 0.4 km^3 × 0.4 km^3 × 0. km^3, and the top of the anomaly body is located at 0.2 km depth. The resistivities of the background, conductive anomaly, resistive anomaly, and air are 100, 10, 1000, and 10^8 Ωm, respectively.

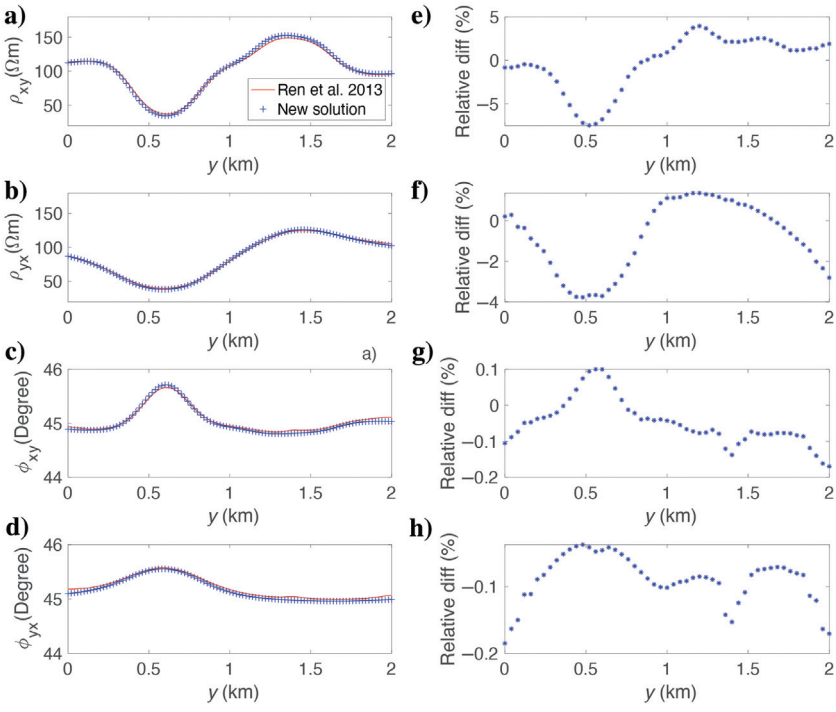

Figure 6. Apparent resistivities and phases at the frequency of 0.1 Hz calculated via the proposed algorithm and the algorithm of Ren et al. (2013) along the x-axis: (a) ρ_{xy}, (b) φ_{xy}, (c) ρ_{yx}, and (d) φ_{yx}. The corresponding relative differences of the two solutions are shown in (e–h). The differences generally are within 5% except at a few data points.

One advantage of the proposed algorithm is that large padding to account for boundary conditions is unnecessary. In this case, our model size is only 2 km^3 × 2 km^3 × 1.4 km^3. This is because all of the horizontal information of the proposed algorithm is in the Fourier domain, and the Gauss FFT can remove the edge effect implicitly. In contrast, the model used by Ren et al. (2013) expands the model region to 140 km^3 × 140 km^3 × 140 km^3. Even though 322,620 elements are used in the algorithm of Ren et al. (2013) after 15 iterations due to the efficiency of the adaptive FEM, a larger number of elements is needed by using other FE methods to discretize such a model. However, the proposed algorithm transforms the 3D problem into 1D problems to reduce memory demand and even has a higher efficiency than the algorithm of Ren et al. (2013).

Model 3: Comparison with a nonadaptive FEM algorithm

To further test the computational efficiency advantage of this algorithm, a large mesh is designed for a 3D model with a quasi-spherical anomaly (Figure 7). The model is discretized into 251 × 251 × 151 nodes and occupies a region of 5 km^3 × 5 km^3 × 3 km^3. A resistive spherical anomaly, 1000 Ωm, with a radius of 0.4 km is buried at 1.4 km depth (Figure 7). Surrounding the sphere is a 100 Ωm half-space. We compare the algorithm with the one of Jahandari and Farquharson (2017), who use an edge-based FEM but with tetrahedral elements. After careful tests, 6.98 million elements are required for the algorithm of Jahandari and Farquharson (2017) to provide an accurate modeling result at the observational locations (251 × 251) in this example. With the goal-oriented adaptive FEM algorithm (Ren et al., 2013), the number of elements in the final iteration should be smaller than the algorithm of Jahandari and Farquharson (2017). However, the price of generating such efficient

discretization is to iterate the modeling, which is not avoidable with goal-oriented adaptive FEM.

The responses at 1 Hz have been modeled with the proposed algorithm using the Gauss FFT method with the two-node Gaussian quadrature rule and with the algorithm of Jahandari and Farquharson (2017), respectively. The responses cannot be further improved after 11 iterations for the proposed method, and no iteration is required for the algorithm of Jahandari and Farquharson (2017). The apparent resistivities and phases at ground level show a resistor beneath the observational surface (Figure 8). Because the MT data are not sensitive to resistors, the maximum apparent resistivity of ρ_{xy} and ρ_{yx} is only 103 Ωm in both results. The spatial FE results are not completely symmetric due to the unstructured mesh generation with TetGen (Si, 2015). In addition, rectilinear grids generally result in smoother patterns in the data. However, the relative differences, $|V_{\text{new}} - V_{\text{FEM}}|/V_{\text{FEM}}$, of the two results are small in Figure 8 (<0.4% in apparent resistivities and phases). Even though the anomaly is approximately spherical, the example shows the potential of our method to handle complex 3D models with a fine discretization.

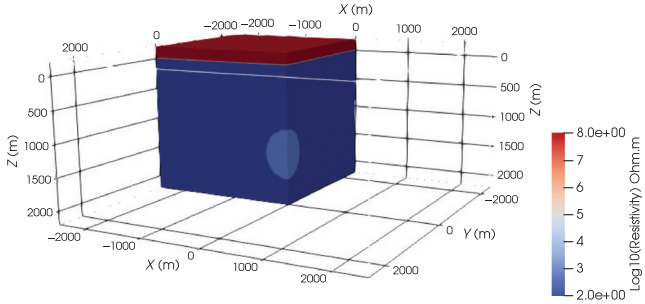

Figure 7. A sphere model used for the modeling efficiency study. Paraview is used for visualization (Ayachit, 2020). Only one-quarter of the model is shown for ease of visual inspection. The anomaly is an approximate sphere with a radius of approximately 0.4 km. Its resistivity is 1000 Ωm. The resistivities of the background and air are 100 and 10^8 Ωm, respectively.

This example also demonstrates the efficiency advantages of the proposed method. With the proposed method, single-frequency EM fields for 251 × 251 observation points are computed using the Gauss FFT method in 1858 s with only four cores, and the largest memory requirement in the entire calculation is 4.9 GB. However, with the use of MUMPS, the algorithm of Jahandari and Farquharson (2017) requires 25,750 s computation time and 202 GB memory in total for four Intel(R) Xeon cores with 2.2 GHz main frequency. Hence, our proposed algorithm can quickly compute the EM fields for large-scale models in comparison with the algorithm of Jahandari and Farquharson (2017) and can promisingly be used for the 3D MT inversion problem based on either deterministic schemes or probabilistic schemes, such as the Bayesian method with a realistic model. The larger the meshing scale, the more obvious the computational efficiency of the algorithm for the 3D MT numerical simulation (highly speculated the same for ERT and CSEM methods). In addition, if the standard FFT with grid expansion is used rather than the Gauss FFT, the calculation efficiency can be further improved (Dai et al., 2019). However, grid expansion requires several attempts to set up a sufficient expansion area to guarantee the accuracy.

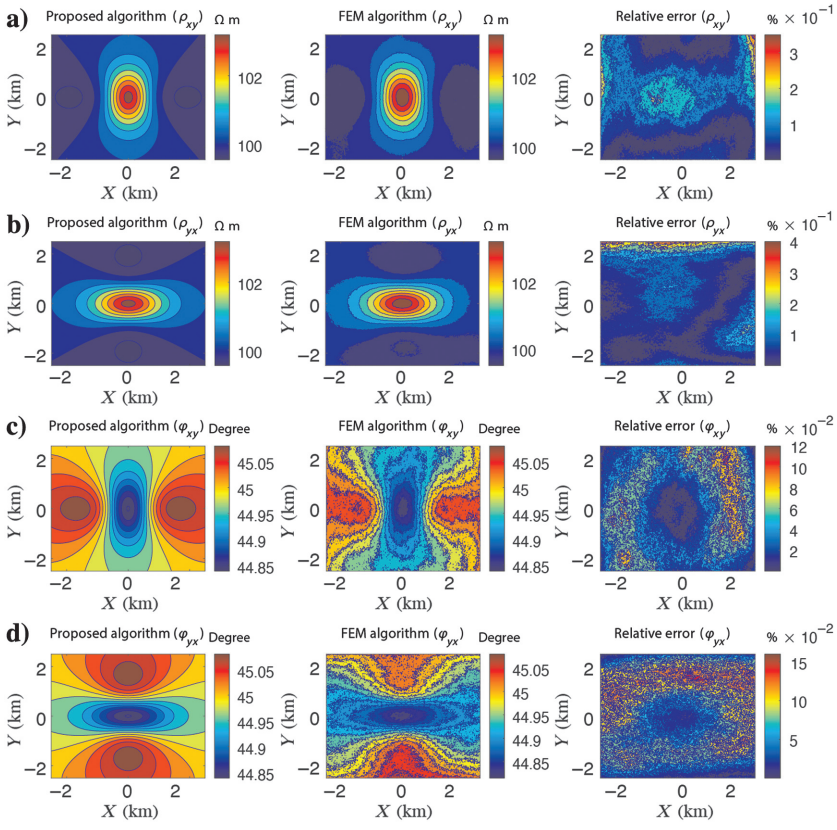

Figure 8. Apparent resistivities and phases at the frequency of 1 Hz calculated via the proposed algorithm, the FEM algorithm of Jahandari and Farquharson (2017), and the relative differences of the two along the plane of $z = 0$: (a) ρ_{xy}, (b) ρ_{yx}, (c) φ_{xy}, and (d) φ_{yx}. The relative differences are smaller than typical noise levels in field data.

CONCLUSION

A new 3D MT modeling algorithm in a mixed space-wavenumber domain is implemented and presented in this study. The accuracy and efficiency of the newly proposed method are verified with three synthetic 3D models by the comparison with a classical IE solution and two well-tested FEM solutions.

The algorithm that transforms the 3D spatial PDEs of the vector-scalar potentials into 1D equations using Fourier transform along horizontal directions can give sufficient accuracy and substantial computational advantages over other published modeling methods. Our method mitigates the memory requirement by approximately 94% and 75% in the second and third synthetic tests, respectively. This indicates that the more complexity a model has, the more memory requirement reduction the method provides. The FEM, together with the chasing method, can solve the 1D vector-scalar potential equations containing different wavenumbers, and the simulation effi-

ciency is improved due to the parallelism among different wavenumbers and the dimensionality reduction. The new algorithm is approximately 8–12 times faster than other FEM algorithms, suggesting that our method is a good candidate for the Bayesian inversion. Because the primary-secondary field separation strategy is applied in our method, extra consideration is needed for including topography, such as calculating the responses of topography numerically. It is worth mentioning that the method also can be used for ERT and CSEM 3D modeling with source inclusion.

ACKNOWLEDGMENTS

The study was supported by the Natural Science Foundation of China (grant no. 41574127) and the Natural Science Foundation of Guangxi Province (grant no. GXNSFGA380004). S. Wang was funded by the Norwegian Research Council together with the industry partners of the GAMES consortium and the Center of Geophysical Forecasting at Norwegian University of Science and Technology (grant nos. 294404, 309960, and 324442). Partial computations were performed on resources provided by Sigma2 — the National Infrastructure for High-Performance Computing and Data Storage in Norway. We appreciate C. G. Farquharson and two anonymous reviewers for their constructive comments. The associate editor X. Hu and the editor J. Etgen also are appreciated for their suggestions to improve this paper.

DATA AND MATERIALS AVAILABILITY

Data associated with this research are available and can be obtained by contacting the corresponding author.

APPENDIX A

BOUNDARY CONDITIONS

In a homogeneous medium, the EM fields satisfy the following Helmholtz equation:

$$\frac{\partial^2 \mathbf{E}^s}{\partial x^2}+\frac{\partial^2 \mathbf{E}^s}{\partial y^2}+\frac{\partial^2 \mathbf{E}^s}{\partial z^2}+k^2\mathbf{E}^s=0. \tag{A-1}$$

The 2D Fourier transform in x- and y-directions is used to express equation A-1 into the mixed space-wavenumber domain; then, we obtain

$$\frac{\partial^2 \tilde{\mathbf{E}}^s}{\partial z^2}-s^2\tilde{\mathbf{E}}^s=0, \tag{A-2}$$

where $s^2=k_x^2+k_y^2-k^2$ will be used for compactness of notation. There is only a downward traveling wave at the lower boundary based on the propagation law of EM waves:

$$\frac{\partial \tilde{\mathbf{E}}^s}{\partial z}=-s\tilde{\mathbf{E}}^s. \tag{A-3}$$

Equation A-3 can be written into the subequation form:

$$\begin{cases}\frac{\partial \tilde{E}_x^s}{\partial z}=-s\tilde{E}_x^s\\ \frac{\partial \tilde{E}_y^s}{\partial z}=-s\tilde{E}_y^s\end{cases}. \tag{A-4}$$

Meanwhile, applying the 2D Fourier transform to equation 4, we obtain

$$\begin{cases}\tilde{E}_x^s=i\omega\tilde{A}_x^s+ik_x\tilde{\Phi}^s\\ \tilde{E}_y^s=i\omega\tilde{A}_y^s+ik_y\tilde{\Phi}^s\\ \tilde{E}_z^s=i\omega\tilde{A}_z^s-\partial\tilde{\Phi}^s/\partial z\end{cases}. \tag{A-5}$$

Through replacing the electric field with $\tilde{E}_x^s$ and $\tilde{E}_y^s$ in equation A-5, equation A-4 can be rewritten as

$$\begin{cases}\frac{\partial \tilde{A}_x^s}{\partial z}=-s\tilde{A}_x^s-\frac{sk_x\tilde{\Phi}^s}{\omega}-\frac{k_x}{\omega}\frac{\partial\tilde{\Phi}^s}{\partial z}\\ \frac{\partial \tilde{A}_y^s}{\partial z}=-s\tilde{A}_y^s-\frac{sk_y\tilde{\Phi}^s}{\omega}-\frac{k_y}{\omega}\frac{\partial\tilde{\Phi}^s}{\partial z}\end{cases}. \tag{A-6}$$

Similarly, applying the 2D Fourier transform to the Coulomb-gauge formulation $\nabla\cdot\mathbf{A}=0$, we obtain

$$\frac{\partial \tilde{A}_z^s}{\partial z}=ik_x\tilde{A}_x^s+ik_y\tilde{A}_y^s. \tag{A-7}$$

In a homogeneous medium, the scalar potential (Φ) satisfies the following equation:

$$\frac{\partial^2\Phi^s}{\partial x^2}+\frac{\partial^2\Phi^s}{\partial y^2}+\frac{\partial^2\Phi^s}{\partial z^2}=0. \tag{A-8}$$

Meanwhile, applying the 2D Fourier transform to equation A-8, we obtain

$$\frac{\partial^2\tilde{\Phi}^s}{\partial z^2}-t^2\tilde{\Phi}^s=0, \tag{A-9}$$

where $t^2=k_x^2+k_y^2$ is used for convenience. Similarly, the lower boundary conditions of the scalar potential in a mixed space-wavenumber domain can be obtained:

$$\frac{\partial\tilde{\Phi}^s}{\partial z}=-t\tilde{\Phi}^s. \tag{A-10}$$

The lower boundary conditions used in the modeling approach can be described as

$$\begin{cases}\frac{\partial \tilde{A}_x^s}{\partial z}=-s\tilde{A}_x^s+\frac{(t-s)}{\omega}k_x\tilde{\Phi}^s\\ \frac{\partial \tilde{A}_y^s}{\partial z}=-s\tilde{A}_y^s+\frac{(t-s)}{\omega}k_y\tilde{\Phi}^s\\ \frac{\partial \tilde{A}_z^s}{\partial z}=ik_x\tilde{A}_x^s+ik_y\tilde{A}_y^s\\ \frac{\partial\tilde{\Phi}^s}{\partial z}=-t\tilde{\Phi}^s\end{cases}. \tag{A-11}$$

The upper boundary conditions can be obtained by the same derivation method:

$$\begin{cases} \frac{\partial \tilde{A}_x^s}{\partial z} = s\tilde{A}_x^s - ik_x\tilde{A}_z^s + \frac{sk_x\tilde{\Phi}^s}{\omega} \\ \frac{\partial \tilde{A}_y^s}{\partial z} = s\tilde{A}_y^s - ik_y\tilde{A}_z^s + \frac{sk_y\tilde{\Phi}^s}{\omega} \\ \frac{\partial \tilde{A}_z^s}{\partial z} = ik_x\tilde{A}_x^s + ik_y\tilde{A}_y^s \\ \frac{\partial \tilde{\Phi}^s}{\partial z} = i\omega\tilde{A}_z^s \end{cases}. \tag{A-12}$$

APPENDIX B

THE EQUIVALENCE BETWEEN VARIATIONAL PROBLEM AND BOUNDARY VALUE PROBLEM

The Galerkin method is used on the vector potential ($\tilde{\mathbf{A}}$) and scalar potential ($\tilde{\Phi}$) system of equations (Xu, 1994; Jin, 2015), and we can obtain the margin equation:

$$\begin{cases} R_{e1} = \frac{\partial^2 \tilde{A}_x^s}{\partial z^2} + (k_p^2 - k_x^2 - k_y^2)\tilde{A}_x^s + ik_x\mu_0\tilde{\sigma}^p\tilde{\Phi}^s + \mu_0\tilde{j}_x^s \\ R_{e2} = \frac{\partial^2 \tilde{A}_y^s}{\partial z^2} + (k_p^2 - k_x^2 - k_y^2)\tilde{A}_y^s + ik_y\mu_0\tilde{\sigma}^p\tilde{\Phi}^s + \mu_0\tilde{j}_y^s \\ R_{e3} = \frac{\partial^2 \tilde{A}_z^s}{\partial z^2} + (k_p^2 - k_x^2 - k_y^2)\tilde{A}_z^s - \tilde{\sigma}^p\mu_0\frac{\partial \tilde{\Phi}^s}{\partial z} + \mu_0\tilde{j}_z^s \\ R_{e4} = (\tilde{\sigma}^p\frac{\partial^2\tilde{\Phi}^s}{\partial z^2} + \frac{\partial\tilde{\sigma}^p}{\partial z}\frac{\partial\tilde{\Phi}^s}{\partial z} - \tilde{\sigma}^p(k_x^2 + k_y^2)\tilde{\Phi}^s) \\ -i\omega\tilde{A}_z^s\frac{\partial\tilde{\sigma}^p}{\partial z} + ik_xj_x^s + ik_yj_y^s - \frac{\partial\tilde{j}_z^s}{\partial z} \end{cases}. \tag{B-1}$$

Letting the weighted integral of equation B-1 in the whole integral region be zero, we obtain

$$\begin{cases} \int_\Omega N_iR_{e1}dz = \sum_{e=1}^{Ne}\int_e N_iR_{e1}dz = 0 \\ \int_\Omega N_iR_{e2}dz = \sum_{e=1}^{Ne}\int_e N_iR_{e2}dz = 0 \\ \int_\Omega N_iR_{e3}dz = \sum_{e=1}^{Ne}\int_e N_iR_{e3}dz = 0 \\ \int_\Omega N_iR_{e4}dz = \sum_{e=1}^{Ne}\int_e N_iR_{e4}dz = 0 \end{cases}, \tag{B-2}$$

where Ω is the integral area, Ne is the number of vertical elements, $N_i(i = j, p, m)$ is the second-order interpolation function, and the specific expressions can be described as (Xu, 1994)

$$N_j = (2L_j - 1)L_j, \quad N_p = 4L_jL_m, \quad N_m = (2L_m - 1)L_m \tag{B-3}$$

and

$$L_j(z) = \frac{z_m - z}{z_m - z_j} = \frac{l_j}{l}, \qquad L_m(z) = \frac{z - z_j}{z_m - z_j} = \frac{l_m}{l}. \tag{B-4}$$

Here, z_j and z_m are the global coordinates in the vertical direction under the Cartesian coordinate system (Figure B-1).

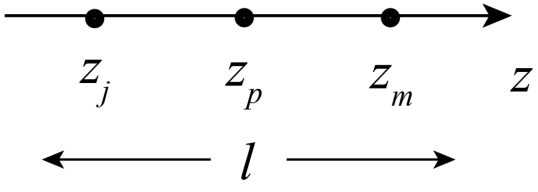

Figure B-1. Length scheme.

Substituting margin equation B-1 into equation B-2, we obtain

$$\begin{cases} \sum_{e=1}^{Ne}\int_e N_i\left(\frac{\partial^2\tilde{A}_x^s}{\partial z^2} + (k_p^2 - k_x^2 - k_y^2)\tilde{A}_x^s + ik_x\mu_0\tilde{\sigma}^p\tilde{\Phi}^s + \mu_0\tilde{j}_x^s\right)dz = 0 \\ \sum_{e=1}^{Ne}\int_e N_i\left(\frac{\partial^2\tilde{A}_y^s}{\partial z^2} + (k_p^2 - k_x^2 - k_y^2)\tilde{A}_y^s + ik_y\mu_0\tilde{\sigma}^p\tilde{\Phi}^s + \mu_0\tilde{j}_y^s\right)dz = 0 \\ \sum_{e=1}^{Ne}\int_e N_i\left(\frac{\partial^2\tilde{A}_z^s}{\partial z^2} + (k_p^2 - k_x^2 - k_y^2)\tilde{A}_z^s - \tilde{\sigma}^p\mu_0\frac{\partial\tilde{\Phi}^s}{\partial z} + \mu_0\tilde{j}_z^s\right)dz = 0 \\ \sum_{e=1}^{Ne}\int_e\left(N_i\left(\tilde{\sigma}^p\frac{\partial^2\tilde{\Phi}^s}{\partial z^2} + \frac{\partial\tilde{\sigma}^p}{\partial z}\frac{\partial\tilde{\Phi}^s}{\partial z} - \tilde{\sigma}^p(k_x^2 + k_y^2)\tilde{\Phi}^s\right)dz\right) + \\ \sum_{e=1}^{Ne}\int_e N_i\left(-i\omega\tilde{A}_z^s\frac{\partial\tilde{\sigma}^p}{\partial z}\right) + N_i\left(ik_xj_x^s + ik_yj_y^s - \frac{\partial\tilde{j}_z^s}{\partial z}\right)dz = 0 \end{cases}. \tag{B-5}$$

The Green's integral formula can be written as

$$\int_e \phi\frac{\partial\varphi}{\partial z}dz = -\int_e \varphi\frac{\partial\phi}{\partial z}dz + \oint_{\partial e}\varphi\phi n_z dl. \tag{B-6}$$

Using Green's formula B-6 to reduce each term of equation B-5, we obtain

$$\begin{cases} \int_e N_i\frac{\partial^2\tilde{A}_x^s}{\partial z^2}dz = -\int_e\frac{\partial\tilde{A}_x^s}{\partial z}\frac{\partial N_i}{\partial z}dz + \int_s N_i\frac{\partial\tilde{A}_x^s}{\partial z}n_z dz \\ \int_e N_i\frac{\partial^2\tilde{A}_y^s}{\partial z^2}dz = -\int_e\frac{\partial\tilde{A}_y^s}{\partial z}\frac{\partial N_i}{\partial z}dz + \int_s N_i\frac{\partial\tilde{A}_y^s}{\partial z}n_z dz \\ \int_e N_i\frac{\partial^2\tilde{A}_z^s}{\partial z^2}dz = -\int_e\frac{\partial\tilde{A}_z^s}{\partial z}\frac{\partial N_i}{\partial z}dz + \int_s N_i\frac{\partial\tilde{A}_z^s}{\partial z}n_z dz \\ \int_e N_i\frac{\partial\tilde{\sigma}^p}{\partial z}\frac{\partial\tilde{\Phi}^s}{\partial z}dz = -\int_e\tilde{\sigma}^p\frac{\partial\tilde{\Phi}^s}{\partial z}\frac{\partial N_i}{\partial z}dz + \int_s\tilde{\sigma}^p\frac{\partial\tilde{\Phi}^s}{\partial z}N_in_z dz \end{cases}. \tag{B-7}$$

Therefore, the final coupled equations required to be solved are

$$\begin{cases} \sum_{e=1}^{Ne}\int_e\left(-\frac{\partial\tilde{A}_x^s}{\partial z}\frac{\partial N_i}{\partial z} + (k_p^2 - k_x^2 - k_y^2)N_i\tilde{A}_x^s + ik_x\mu_0\tilde{\sigma}^pN_i\tilde{\Phi}^s + N_i\mu_0\tilde{j}_x^s\right)dz \\ + \sum_{e=1}^{Ne}\int_s N_i\frac{\partial\tilde{A}_x^s}{\partial z}n_z dz = 0 \\ \sum_{e=1}^{Ne}\int_e\left(-\frac{\partial\tilde{A}_y^s}{\partial z}\frac{\partial N_i}{\partial z} + (k_p^2 - k_x^2 - k_y^2)N_i\tilde{A}_y^s + ik_y\mu_0\tilde{\sigma}^pN_i\tilde{\Phi}^s + N_i\mu_0\tilde{j}_y^s\right)dz \\ + \sum_{e=1}^{Ne}\int_s N_i\frac{\partial\tilde{A}_y^s}{\partial z}n_z dz = 0 \\ \sum_{e=1}^{Ne}\int_e\left(-\frac{\partial\tilde{A}_z^s}{\partial z}\frac{\partial N_i}{\partial z} + (k_p^2 - k_x^2 - k_y^2)N_i\tilde{A}_z^s - \mu_0\tilde{\sigma}^pN_i\frac{\partial\tilde{\Phi}^s}{\partial z} + N_i\mu_0\tilde{j}_z^s\right)dz \\ + \sum_{e=1}^{Ne}\int_s N_i\frac{\partial\tilde{A}_z^s}{\partial z}n_z dz = 0 \\ \sum_{e=1}^{Ne}\int_e\left(-\tilde{\sigma}^p\frac{\partial\tilde{\Phi}^s}{\partial z}\frac{\partial N_i}{\partial z} + N_i\frac{\partial\tilde{\sigma}^p}{\partial z}\frac{\partial\tilde{\Phi}^s}{\partial z} - \tilde{\sigma}^p(k_x^2 + k_y^2)N_i\tilde{\Phi}^s\right)dz + \\ \sum_{e=1}^{Ne}\int_e\left(-i\omega N_i\frac{\partial\tilde{\sigma}^p}{\partial z}\tilde{A}_z^s + ik_xN_i\tilde{j}_x^s + ik_yN_i\tilde{j}_y^s - N_i\frac{\partial\tilde{j}_z^s}{\partial z}\right)dz + \\ \sum_{e=1}^{Ne}\int_s\tilde{\sigma}^pN_i\frac{\partial\tilde{\Phi}^s}{\partial z}n_z dz = 0 \end{cases}. \tag{B-8}$$

APPENDIX C

FINITE-ELEMENT ANALYSIS

The vector and scalar potentials in equation 17 are expressed as a second-order interpolation function:

$$\begin{cases} \tilde{\Phi}^s = \sum_{i=1}^3 N_i \tilde{\Phi}_i^s \\ \tilde{A}_x^s = \sum_{i=1}^3 N_i \tilde{A}_{xi}^s \\ \tilde{A}_y^s = \sum_{i=1}^3 N_i \tilde{A}_{yi}^s \\ \tilde{A}_z^s = \sum_{i=1}^3 N_i \tilde{A}_{zi}^s \\ \hat{y}_p = \sum_{i=1}^3 N_i \hat{y}_{pi} \\ \tilde{J}_z^s = \sum_{i=1}^3 N_i \tilde{J}_{zi} \end{cases} \quad i = 1, 2, 3. \tag{C-1}$$

Substituting equation C-1 into equation 17, equation 18 can be formed by finite-element analysis. The following seven types of integral cover all integral types of equation 17, and other integral terms can be found in these seven types of integral.

1) The first element integral form in equation 17 is

$$\int_e \frac{\partial \tilde{A}_x^s}{\partial z}\frac{\partial N_i}{\partial z} dz = \mathbf{K_{1e}}\tilde{A}_{xe}^s = \frac{1}{3l}\begin{pmatrix} 7 & -8 & 1 \\ -8 & 16 & -8 \\ 1 & -8 & 7 \end{pmatrix}\begin{pmatrix} \tilde{A}_{xj}^s \\ \tilde{A}_{xp}^s \\ \tilde{A}_{xm}^s \end{pmatrix}. \tag{C-2}$$

2) The second element integral form in equation 17 is

$$\int_e N_i \tilde{A}_x^s dz = \mathbf{K_{2e}}\tilde{A}_{xe}^s = \frac{l}{30}\begin{pmatrix} 4 & 2 & -1 \\ 2 & 16 & 2 \\ -1 & 2 & 4 \end{pmatrix}\begin{pmatrix} \tilde{A}_{xj}^s \\ \tilde{A}_{xp}^s \\ \tilde{A}_{xm}^s \end{pmatrix}. \tag{C-3}$$

3) The third element integral form in equation 17 is

$$\int_e N_i \frac{\partial \tilde{A}_x^s}{\partial z} dz = \mathbf{K_{3e}}\tilde{A}_x^s = \frac{1}{6}\begin{pmatrix} -3 & 4 & -1 \\ -4 & 0 & 4 \\ 1 & -4 & 3 \end{pmatrix}\begin{pmatrix} \tilde{A}_{xi}^s \\ \tilde{A}_{xj}^s \\ \tilde{A}_{xm}^s \end{pmatrix}. \tag{C-4}$$

4) The fourth element integral form in equation 17 is

$$\int_e N_i \frac{\partial \tilde{\sigma}^p}{\partial z}\tilde{A}_z^s dz = \mathbf{K_{4e}}\tilde{A}_{ze}^s = \frac{l}{30}\begin{pmatrix} k_{11}^{4e} & k_{12}^{4e} & k_{13}^{4e} \\ k_{21}^{4e} & k_{22}^{4e} & k_{23}^{4e} \\ k_{31}^{4e} & k_{32}^{4e} & k_{33}^{4e} \end{pmatrix}\begin{pmatrix} \tilde{A}_{zj}^s \\ \tilde{A}_{zp}^s \\ \tilde{A}_{zm}^s \end{pmatrix}, \tag{C-5}$$

where $k_{11}^{4e} = -10\tilde{\sigma}_j^p + 12\tilde{\sigma}_p^p - 2\tilde{\sigma}_m^p$, $k_{12}^{4e} = -6\tilde{\sigma}_j^p + 8\tilde{\sigma}_p^p - 2\tilde{\sigma}_m^p$, $k_{13}^{4e} = \tilde{\sigma}_j^p - \tilde{\sigma}_m^p$, $k_{21}^{4e} = -6\tilde{\sigma}_j^p + 8\tilde{\sigma}_p^p - 2\tilde{\sigma}_m^p$, $k_{22}^{4e} = -16\tilde{\sigma}_j^p + 16\tilde{\sigma}_m^p$, $k_{23}^{4e} = 2\tilde{\sigma}_j^p - 8\tilde{\sigma}_p^p + 6\tilde{\sigma}_m^p$, $k_{31}^{4e} = \tilde{\sigma}_j^p - \tilde{\sigma}_m^p$, $k_{32}^{4e} = 2\tilde{\sigma}_j^p - 8\tilde{\sigma}_p^p + 6\tilde{\sigma}_m^p$, and $k_{33}^{4e} = 2\tilde{\sigma}_j^p - 12\tilde{\sigma}_p^p + 10\tilde{\sigma}_m^p$.

5) The fifth element integral form in equation 17 is

$$\int_e \tilde{\sigma}^p \tilde{\Phi}^s N_i dz = \mathbf{K_{5e}}\tilde{A}_{ze}^s = \frac{l}{420}\begin{pmatrix} k_{11}^{5e} & k_{12}^{5e} & k_{13}^{5e} \\ k_{21}^{5e} & k_{22}^{5e} & k_{23}^{5e} \\ k_{31}^{5e} & k_{32}^{5e} & k_{33}^{5e} \end{pmatrix}\begin{pmatrix} \tilde{\Phi}_j^s \\ \tilde{\Phi}_p^s \\ \tilde{\Phi}_m^s \end{pmatrix}, \tag{C-6}$$

where $k_{11}^{5e} = 39\tilde{\sigma}_j^p + 20\tilde{\sigma}_p^p - 3\tilde{\sigma}_m^p$, $k_{12}^{5e} = 20\tilde{\sigma}_j^p + 16\tilde{\sigma}_p^p - 8\tilde{\sigma}_m^p$, $k_{13}^{5e} = -3\tilde{\sigma}_j^p - 8\tilde{\sigma}_p^p - 3\tilde{\sigma}_m^p$, $k_{21}^{5e} = 20\tilde{\sigma}_j^p + 16\tilde{\sigma}_p^p - 8\tilde{\sigma}_m^p$, $k_{22}^{5e} = 16\tilde{\sigma}_j^p + 192\tilde{\sigma}_p^p + 16\tilde{\sigma}_m^p$, $k_{23}^{5e} = -8\tilde{\sigma}_j^p + 16\tilde{\sigma}_p^p + 20\tilde{\sigma}_m^p$, $k_{31}^{5e} = -3\tilde{\sigma}_j^p - 8\tilde{\sigma}_p^p - 3\tilde{\sigma}_m^p$, $k_{32}^{5e} = -8\tilde{\sigma}_j^p + 16\tilde{\sigma}_p^p + 20\tilde{\sigma}_m^p$, and $k_{33}^{5e} = -3\tilde{\sigma}_j^p + 20\tilde{\sigma}_p^p + 39\tilde{\sigma}_m^p$.

6) The sixth element integral form in equation 17 is

$$\int_e N_i \frac{\partial \tilde{\sigma}^p}{\partial z}\frac{\partial \tilde{\Phi}^s}{\partial z} dz = \mathbf{K_{6e}}\tilde{\Phi}_e^s = \frac{1}{30l}\begin{pmatrix} k_{11}^{6e} & k_{12}^{6e} & k_{13}^{6e} \\ k_{21}^{6e} & k_{22}^{6e} & k_{23}^{6e} \\ k_{31}^{6e} & k_{32}^{6e} & k_{33}^{6e} \end{pmatrix}\begin{pmatrix} \tilde{\Phi}_j^s \\ \tilde{\Phi}_p^s \\ \tilde{\Phi}_m^s \end{pmatrix}, \tag{C-7}$$

where $k_{11}^{6e} = 37\tilde{\sigma}_j^p + 36\tilde{\sigma}_p^p - 3\tilde{\sigma}_m^p$, $k_{12}^{6e} = -6\tilde{\sigma}_j^p + 8\tilde{\sigma}_p^p - 2\tilde{\sigma}_m^p$, $k_{13}^{6e} = -6\tilde{\sigma}_j^p + 8\tilde{\sigma}_p^p - 2\tilde{\sigma}_m^p$, $k_{21}^{6e} = -44\tilde{\sigma}_j^p - 32\tilde{\sigma}_p^p - 4\tilde{\sigma}_m^p$, $k_{22}^{6e} = 48\tilde{\sigma}_j^p + 64\tilde{\sigma}_p^p + 48\tilde{\sigma}_m^p$, $k_{23}^{6e} = 2\tilde{\sigma}_j^p - 8\tilde{\sigma}_p^p + 6\tilde{\sigma}_m^p$, $k_{31}^{6e} = 7\tilde{\sigma}_j^p - 4\tilde{\sigma}_p^p + 7\tilde{\sigma}_m^p$, $k_{32}^{6e} = -4\tilde{\sigma}_j^p - 32\tilde{\sigma}_p^p - 44\tilde{\sigma}_m^p$, and $k_{33}^{6e} = -3\tilde{\sigma}_j^p + 36\tilde{\sigma}_p^p + 37\tilde{\sigma}_m^p$.

7) The seventh element integral form in equation 17 is

$$\int_e \tilde{\sigma}^p N_i \frac{\partial \tilde{\Phi}^s}{\partial z} dz = \mathbf{K_{7e}}\tilde{\Phi}_e^s = \frac{1}{30}\begin{pmatrix} k_{11}^{7e} & k_{12}^{7e} & k_{13}^{7e} \\ k_{21}^{7e} & k_{22}^{7e} & k_{23}^{7e} \\ k_{31}^{7e} & k_{32}^{7e} & k_{33}^{7e} \end{pmatrix}\begin{pmatrix} \tilde{\Phi}_j^s \\ \tilde{\Phi}_p^s \\ \tilde{\Phi}_m^s \end{pmatrix}, \tag{C-8}$$

where $k_{11}^{7e} = -10\tilde{\sigma}_j^p - 6\tilde{\sigma}_p^p + \tilde{\sigma}_m^p$, $k_{12}^{7e} = 12\tilde{\sigma}_j^p + 8\tilde{\sigma}_p^p$, $k_{13}^{7e} = -2\tilde{\sigma}_j^p - 2\tilde{\sigma}_p^p - \tilde{\sigma}_m^p$, $k_{21}^{7e} = -6\tilde{\sigma}_j^p - 16\tilde{\sigma}_p^p + 2\tilde{\sigma}_m^p$, $k_{22}^{7e} = 8\tilde{\sigma}_j^p - 8\tilde{\sigma}_m^p$, $k_{23}^{7e} = -2\tilde{\sigma}_j^p + 16\tilde{\sigma}_p^p + 6\tilde{\sigma}_m^p$, $k_{31}^{7e} = 7\tilde{\sigma}_j^p - 4\tilde{\sigma}_p^p + 7\tilde{\sigma}_m^p$, $k_{32}^{7e} = -8\tilde{\sigma}_p^p - 12\tilde{\sigma}_m^p$, and $k_{33}^{7e} = -\tilde{\sigma}_j^p + 6\tilde{\sigma}_p^p + 10\tilde{\sigma}_m^p$.

REFERENCES

Ansari, S., and C. Farquharson, 2014, 3D finite-element forward modeling of electromagnetic data using vector and scalar potentials and unstructured grids: Geophysics, **79**, no. 4, E149–E165, doi: 10.1190/geo2013-0172.1.

Avdeev, D., and A. Avdeeva, 2009, 3D magnetotelluric inversion using a limited-memory quasi-Newton optimization: Geophysics, **74**, no. 3, F45–F57, doi: 10.1190/1.3114023.

Avdeev, D. B., A. V. Kuvshinov, O. V. Pankratov, and G. A. Newman, 1997, High-performance three-dimensional electromagnetic modelling using modified Neumann series. Wide-band numerical solution and examples: Journal of Geomagnetism and Geoelectricity, **49**, 1519–1539, doi: 10.5636/jgg.49.1519.

Avdeev, D. B., A. V. Kuvshinov, O. V. Pankratov, and G. A. Newman, 2002, Three-dimensional induction logging problems, Part I: An integral equation solution and model comparisons: Geophysics, **67**, 413–426, doi: 10.1190/1.1468601.

Ayachit, U., 2020, The ParaView guide: Kitware, Inc., 276.

Badea, E. A., M. E. Everett, G. A. Newman, and O. Biro, 2001, Finite-element analysis of controlled-source electromagnetic induction using Coulomb-gauged potentials: Geophysics, **66**, 786–799, doi: 10.1190/1.1444968.

Boisvert, R. F., 1991, Algorithms for special tridiagonal systems: Society for Industrial and Applied Mathematics, **12**, 423–442, doi: 10.1137/0912023.

Chai, Y., 2009, A-E equation of potential field transformations in the wavenumber domain and its application: Applied Geophysics, **6**, 205–216, doi: 10.1007/s11770-009-0032-z.

Chen, H., and T. Li, 2019, 3-D marine controlled-source electromagnetic modelling in an anisotropic medium using a Wavelet–Galerkin method with a secondary potential formulation: Geophysical Journal International, **219**, 373–393, doi: 10.1093/gji/ggz305.

Dai, S., D. Zhao, S. Wang, B. Xiong, Q. Zhang, K. Li, L. Chen, and Q. Chen, 2019, Three-dimensional numerical modeling of gravity and magnetic anomaly in a mixed space-wavenumber domain: Geophysics, **84**, no. 4, G41–G54, doi: 10.1190/geo2018-0491.1.

da Silva, N. V., J. V. Morgan, L. MacGregor, and M. Warner, 2012, A finite element multifrontal method for 3D CSEM modeling in the frequency domain: Geophysics, **77**, no. 2, E101–E115, doi: 10.1190/geo2010-0398.1.

Egbert, G., and A. Kelbert, 2012, Computational recipes for electromagnetic inverse problems: Geophysical Journal International, **189**, 251–267, doi: 10.1111/j.1365-246X.2011.05347.x.

Farquharson, C. G., and M. P. Miensopust, 2011, Three-dimensional finite-element modelling of magnetotelluric data with a divergence correction: Journal of Applied Geophysics, **75**, 699–710, doi: 10.1016/j.jappgeo.2011.09.025.

Franke, A., R.-U. Börner, and K. Spitzer, 2007, 3D finite element simulation of magnetotelluric fields using unstructured grids: Proceedings of the 22nd Colloquium of Electromagnetic Depth Research, 27–33.

Gao, G., 2005, Simulation of borehole electromagnetic measurements in dipping and anisotropic rock formations and inversion of array induction data: Ph.D. thesis, University of Texas.

Grayver, A. V., and T. V. Kolev, 2015, Large-scale 3D geoelectromagnetic modeling using parallel adaptive high-order finite element method EM modeling with high-order FEM: Geophysics, **80**, no. 6, E277–E291, doi: 10.1190/geo2015-0013.1.

Haber, E., and U. M. Ascher, 2001, Fast finite volume simulation of 3D electromagnetic problems with highly discontinuous coefficients: SIAM Journal on Scientific Computing, **22**, 1943–1961, doi: 10.1137/S1064827599360741.

Haber, E., U. M. Ascher, D. A. Aruliah, and D. W. Oldenburg, 2000, Fast simulation of 3D electromagnetic problems using potentials: Journal of Computational Physics, **163**, 150–171, doi: 10.1006/jcph.2000.6545.

Hursán, G., and M. S. Zhdanov, 2002, Contraction integral equation method in three-dimensional electromagnetic modeling: Radio Science, **37**, 1–1-13, doi: 10.1029/2001RS002513.

Jahandari, H., S. Ansari, and C. G. Farquharson, 2017, Comparison between staggered grid finite–volume and edge–based finite–element modelling of geophysical electromagnetic data on unstructured grids: Journal of Applied Geophysics, **138**, 185–197, doi: 10.1016/j.jappgeo.2017.01.016.

Jahandari, H., and C. G. Farquharson, 2014, A finite-volume solution to the geophysical electromagnetic forward problem using unstructured grids: Geophysics, **79**, no. 6, E287–E302, doi: 10.1190/geo2013-0312.1.

Jahandari, H., and C. G. Farquharson, 2015, Finite-volume modelling of geophysical electromagnetic data on unstructured grids using potentials: Geophysical Journal International, **202**, 1859–1876, doi: 10.1093/gji/ggv257.

Jahandari, H., and C. G. Farquharson, 2017, 3-D minimum-structure inversion of magnetotelluric data using the finite-element method and tetrahedral grids: Geophysical Journal International, **211**, 1189–1205, doi: 10.1093/gji/ggx358.

Jin, J.-M., 2015, The finite element method in electromagnetics: John Wiley & Sons.

Key, K., 2016, MARE2DEM: A 2-D inversion code for controlled-source electromagnetic and magnetotelluric data: Geophysical Journal International, **207**, 571–588, doi: 10.1093/gji/ggw290.

Kruglyakov, M., and L. Bloshanskaya, 2016, High-performance parallel solver for integral equations of electromagnetics based on Galerkin method: Mathematical Geosciences, **49**, 751–776, doi: 10.1007/s11004-017-9677-y.

Liu, C., Z. Ren, J. Tang, and Y. Yan, 2008, Three-dimensional magnetotellurics modeling using edge-based finite-element unstructured meshes: Applied Geophysics, **5**, 170–180, doi: 10.1007/s11770-008-0024-4.

Lynch, D. R., and K. D. Paulsen, 1991, Origin of vector parasites in numerical Maxwell solutions: IEEE Transactions on Microwave Theory and Techniques, **39**, 383–394, doi: 10.1109/22.75279.

Mackie, R. L., J. T. Smith, and T. R. Madden, 1994, Three-dimensional electromagnetic modeling using finite difference equations: The magnetotelluric example: Radio Science, **29**, 923–935, doi: 10.1029/94RS00326.

Mitsuhata, Y., and T. Uchida, 2004, 3D magnetotelluric modeling using the T-Ω finite-element method: Geophysics, **69**, 108–119, doi: 10.1190/1.1649380.

Mukherjee, S., and M. E. Everett, 2011, 3D controlled-source electromagnetic edge-based finite element modeling of conductive and permeable heterogeneities: Geophysics, **76**, no. 4, F215–F226, doi: 10.1190/1.3571045.

Nam, M. J., H. J. Kim, Y. Song, T. J. Lee, J.-S. Son, and J. H. Suh, 2007, 3D magnetotelluric modelling including surface topography: Geophysical Prospecting, **55**, 277–287, doi: 10.1111/j.1365-2478.2007.00614.x.

Newman, G., and D. Alumbaugh, 2000, Three-dimensional magnetotelluric inversion using non-linear conjugate gradients: Geophysical Journal International, **140**, 410–424, doi: 10.1046/j.1365-246x.2000.00007.x.

Newman, G. A., and D. L. Alumbaugh, 1995, Frequency-domain modelling of airborne electromagnetic responses using staggered finite differences1: Geophysical Prospecting, **43**, 1021–1042, doi: 10.1111/j.1365-2478.1995.tb00294.x.

Ren, Z., T. Kalscheuer, S. Greenhalgh, and H. Maurer, 2013, A goal-oriented adaptive finite-element approach for plane wave 3-D electromagnetic modelling: Geophysical Journal International, **194**, 700–718, doi: 10.1093/gji/ggt154.

Saad, Y., 2003, Iterative methods for sparse linear systems: SIAM.

Sasaki, Y., 2001, Full 3-D inversion of electromagnetic data on PC: Journal of Applied Geophysics, **46**, 45–54, doi: 10.1016/S0926-9851(00)00038-0.

Shen, J., 2003, Modeling of 3-D electromagnetic responses in frequency domain by using the staggered grid finite difference method: Chinese Journal of Geophysics, **46**, 396–408, doi: 10.1002/cjg2.355.

Si, H., 2015, TetGen, a Delaunay-based quality tetrahedral mesh generator: ACM Transactions on Mathematical Software, **41**, 1–36, doi: 10.1145/2629697.

Smith, J. T., 1996, Conservative modeling of 3-D electromagnetic fields, Part II: Biconjugate gradient solution and an accelerator: Geophysics, **61**, 1319–1324, doi: 10.1190/1.1444055.

Streich, R., 2009, 3D finite-difference frequency-domain modeling of controlled-source electromagnetic data: Direct solution and optimization for high accuracy: Geophysics, **74**, no. 5, F95–F105, doi: 10.1190/1.3196241.

Sugeng, F., 1998, Modeling the 3D TDEM response using the 3D full-domain finite-element method based on the hexahedral edge-element technique: Exploration Geophysics, **29**, 615–619, doi: 10.1071/EG998615.

Temperton, C., 1975, Algorithms for the solution of cyclic tridiagonal systems: Journal of Computational Physics, **19**, 317–323, doi: 10.1016/0021-9991(75)90081-9.

Tontini, F. C., L. Cocchi, and C. Carmisciano, 2009, Rapid 3-D forward model of potential fields with application to the Palinuro Seamount magnetic anomaly (southern Tyrrhenian Sea, Italy): Journal of Geophysical Research: Solid Earth, **114**, B02103, doi: 10.1029/2008JB005907.

Um, E. S., D. L. Alumbaugh, and J. M. Harris, 2010, A Lorenz-gauged finite-element solution for transient CSEM modeling: 80th Annual International Meeting, SEG, Expanded Abstracts, 748–752, doi: 10.1190/1.3513890.

Varentsov, I. M., 1983, Modern trends in the solution of forward and inverse 3D electromagnetic induction problems: Geophysical Surveys, **6**, 55–78, doi: 10.1007/BF01453995.

Varilsuha, D., and M. E. Candansayar, 2018, 3D magnetotelluric modeling by using finite-difference method: Comparison study of different forward modeling approaches: Geophysics, **83**, no. 2, WB51–WB60, doi: 10.1190/geo2017-0406.1.

Wannamaker, P., G. Hohmann, and S. Ward, 1984a, Magnetotelluric responses of three-dimensional bodies in layered earths: Geophysics, **49**, 1517–1533, doi: 10.1190/1.1441777.

Wannamaker, P. E., G. W. Hohmann, and W. A. SanFilipo, 1984b, Electromagnetic modeling of three-dimensional bodies in layered earths using integral equations: Geophysics, **49**, 60–74, doi: 10.1190/1.1441562.

Wu, L., and G. Tian, 2014, High-precision Fourier forward modeling of potential fields: Geophysics, **79**, no. 5, G59–G68, doi: 10.1190/geo2014-0039.1.

Xu, S., 1994, The finite element method in geophysics: Science Press.

Zhdanov, M. S., 2010, Electromagnetic geophysics: Notes from the past and the road ahead: Geophysics, **75**, no. 5, 75A49–75A66, doi: 10.1190/1.3483901.

Zhdanov, M. S., S. K. Lee, and K. Yoshioka, 2006, Integral equation method for 3D modeling of electromagnetic fields in complex structures with inhomogeneous background conductivity: Geophysics, **71**, no. 6, G333–G345, doi: 10.1190/1.2358403.

Zunoubi, M. R., J.-M. Jin, K. C. Donepudi, and W. C. Chew, 1999, A spectral Lanczos decomposition method for solving 3-D low-frequency electromagnetic diffusion by the finite-element method: IEEE Transactions on Antennas and Propagation, **47**, 242–248, doi: 10.1109/8.761063.

Biographies and photographs of the authors are not available.